Title	Effect of quenching on molten core-concrete interaction product
Author(s)	Kitagaki Toru, Ikeuchi Hirotomo, Yano Kimihiko, Brissonneau L., Tormos B., Domenger R., Roger J., Washiya Tadahiro
Citation	Journal of Nuclear Science and Technology,56(9-10),p.902-914
Text Version	Accepted Manuscript
URL	https://jopss.jaea.go.jp/search/servlet/search?5064018
DOI	https://doi.org/10.1080/00223131.2019.1604272
Right	This is an Accepted Manuscript of an article published by Taylor & Francis in Journal of Nuclear Science and Technology on September 2019, available at http://www.tandfonline.com/10.1080/00223131.2019.1604272.

ARTICLE

Effect of quenching on molten core-concrete interaction product

Toru Kitagaki [a,b*], Hirotomo Ikeuchi[a,b], Kimihiko Yano[a,b], Laurent Brissonneau[c], Brigitte Tormos[c], Renaud Domenger[d], Julien Roger[d] and Tadahiro Washiya[a,b]

[a]Japan Atomic Energy Agency, 4-33 Mramatsu, Tokai-mura, Naka-gun, Ibaraki-ken 319-1194, Japan; [b]International Research Institute for Nuclear Decommissioning, 2-23-1 Nishi-Shimbashi, Minato-ku, Tokyo 105-0003, Japan; [c]Commissariat à l'énergie atomique et aux énergies alternatives, Direction de l'énergie nucléaire, Centre de Cadarache, Saint-Paul Lez Durance, 13108, France; [d]Commissariat à l'énergie atomique et aux énergies alternatives, Direction de l'énergie nucléaire, Centre de Marcoule, Bagnols sur Cèze cedex, 30207, France

Acknowledgments

The VULCANO VW-U1 experiment was carried out for FZK within the PLINIUS platform Transnational Accesses funded by the European Union under the EURATOM 5th Framework Program contract FIR1-CT-2001-40152. This study includes results obtained under the research program entrusted to the International Research Institute for Nuclear Decommissioning, including the Japan Atomic Energy Agency by the Agency for Natural Resources and Energy, Ministry of Economy, Trade and Industry (METI) of Japan. This work was supported by the Ministry of Economy, Trade and Industry for the Project of Decommissioning and Contaminated Water Management.

Abstract

Characterization of fuel debris is required to develop fuel debris removal tools for decommissioning Fukushima Daiichi nuclear power plant (1F). Especially, knowledge about

*Corresponding author. Email: kitagaki.toru@jaea.go.jp

the characteristics of molten core-concrete interaction (MCCI) product is needed because of the limited information available at present. Samples from a large-scale MCCI test performed under quenching conditions, VULCANO VW-U1, by CEA were analyzed to evaluate the characteristics of the surface of MCCI product generated just below the cooling water in 1F. Four samples were selected from test sections at different locations, and the structure, crystal structure, and Vickers hardness of the samples were analyzed. As a result, the characteristics of the samples were found to be similar, despite the different locations of the test sections. Several corium phases, such as cubic-$(U,Zr)O_2$ and tetragonal ZrO_2, were detected by X-ray diffraction (XRD), but concrete-based phases, such as the crystalline SiO_2 phase, were not detected despite their detection by scanning electron microscopy-energy dispersive X-ray spectroscopy (SEM-EDS) because the quantity of the SiO_2 phase was too small to be measured using XRD. The Vickers hardness of each phase in these samples was higher than that of previously analyzed samples in another VULCANO test campaign, VBS-U4. Based on a comparison between MCCI product generated under quenching condition, such as VW-U1, and gently cooled MCCI product, such as VBS-U4, the MCCI product generated under quenching condition is more homogeneous, and its hardness is higher than that of the gently cooled MCCI product.

Keywords: Fukushima Daiichi Nuclear Power Plant; MCCI; Fuel debris; Mechanical properties; hardness; decommissioning; severe accident

1. Introduction

Fuel debris removal is one of the most important processes for decommissioning the Fukushima Daiichi nuclear power plant (1F), as well as the Three Mile Island nuclear power generation station, unit 2 (TMI-2). Estimation of the characteristics of fuel debris, such as structure and mechanical and thermal properties, is required to develop fuel debris removal tools and achieve efficient debris removal [1]. In the case of 1F unit 1, the molten core in the reactor pressure vessel would have penetrated the bottom of the vessel and reacted with the concrete in the primary containment vessel during the accident [2]. Although the characteristics of the materials produced by molten core-concrete interaction (MCCI) must be estimated, information about such products is limited because there was no MCCI in the TMI-2 accident, and few analytical data pertaining to fuel debris samples picked up from Chernobyl NPP (ChNPP) are available [3-5]. Moreover, the accident progression and concrete composition of ChNPP are drastically different from those of 1F [2, 6]. On the one hand, the characteristics of large-scale MCCI test products and corium-spreading test materials can be useful for evaluating the characteristics of MCCI products. Nevertheless, the mechanical and thermal properties of the samples were not measured because these samples were analyzed from the viewpoint of evaluating accident progression [7-10].

For the abovementioned reasons, the VULCANO VBS-U4 large-scale MCCI test campaign undertaken by CEA is selected because the experimental conditions in that campaign were similar to the MCCI condition at 1F unit 1, and test samples are analyzed to evaluate the characteristics of the 1F MCCI product [11]. On the other hand, although the upper part of the MCCI product in 1F unit 1 could have reacted with cooling water and could have been quenched, the quenching effect of cooling water on the MCCI product was not considered in VULCANO VBS-U4. By contrast, the VULCANO VW-U1 test campaign was performed to validate the bottom-cooling system concept of molten core-concrete [12-13]. The molten core-concrete in the test section is cooled by water at the bottom, and the surface of the test

section is cooled as well. This cooling phenomenon could approximate the quenching process during MCCI in 1F, at least near the surface of molten core-concrete. In the present study, samples obtained in the VW-U1 test campaign are analyzed to obtain knowledge pertaining to their characteristics such as millimeter- and micrometer-scale structure and mechanical properties of quenched oxide materials.

2. Overview of quenched MCCI test and analytical method for test product

2.1. Quenched MCCI test condition and test scenario

The VULCANO VW-U1 test was performed at CEA Cadarache in 2005 by using a cylindrical zirconia crucible measuring 25 cm in diameter and 60 cm in height, and equipped with a passive bottom cooling system comprising three concrete layers, namely, a 20-mm -thick layer of sacrificial concrete composed of ferro-siliceous concrete, 30-mm-thick layer of porous concrete, and structural concrete layer from the top to bottom. The porous concrete layer is connected to the water piping system and filled with water to quench the molten corium. The sacrificial concrete consisted of aggregates of a borosilicate glass with the following average composition: SiO_2 62.5%, B_2O_3 > 6%, Al_2O_3 > 5%, Na_2O 14.5%, CaO 6%, MgO 3.5%, TiO_2 < 1%, Fe_2O_3 < 1%, K_2O >1%, and other impurities < 0.5% [14]. The initial corium load was 45 wt.% UO_2, 19.3 wt.% ZrO_2, 19.6 wt.% SiO_2, 15.3 wt.% FeO_x, 0.7 wt.% CaO, and 0.1 wt.% Al_2O_3. This composition simulated the mixture of corium with a part of a ferro-siliceous sacrificial concrete. Its liquidus temperature was approximately 2130 K, as estimated using GEMINI2 thermodynamic equilibrium calculation software and NUCLEA database version 10. This initial corium was heated using the VULCANO plasma arc furnace to temperatures higher than 2000 K and poured into a zirconia crucible. The poured corium was heated using an induction heating system installed around the zirconia crucible to simulate decay heat until complete cooling was achieved.

Passive water injection from the porous concrete was started approximately 1 min

after the corium was poured, when the top layer of the sacrificial concrete was eroded. Then, the injected water was evaporated, and it quenched the molten corium. The porous concrete remained, and the molten corium was cooled permanently owing to water inflow from the porous concrete. Finally, the molten corium solidified in less than 20 min, and thermocouples installed in the sacrificial concrete indicated that 2 cm of sacrificial concrete was ablated during the experiment. Other details of this experimental setup and test condition can be found in [12].

2.2. Post-test situation and sample location

A simplified schema of a cut view of the VW-U1 spatial repartition, as observed during dismantling of the VW-U1 test section, is shown in figure 1. The product can be classified roughly into two different regions: upper crust region and bulk of molten pool region below the upper crust.

Four samples were selected to represent different interfaces or specific corium melt compositions to cover a wide range of solidified corium materials according to local compositions, spatial repartition, and melting/solidification history under MCCI conditions. The approximate locations are listed below and shown in figure 1.

- Sample A: Left side of upper crust
- Sample B: Center of upper crust
- Sample C: Right side of upper crust
- Sample D: Inner region of molten pool

2.3. Post-test analysis method

Millimeter- and micrometer-scale structural observation and elemental analysis of the samples were performed using a scanning electron microscope EVO HD15MA by Zeiss equipped with an energy-dispersive X-ray spectroscope (SEM-EDS) SDD X-Max 50 by

Oxford Instruments. The cross sections to be analyzed were polished to a mirror finish.

Bulk density and apparent porosity of the samples were measured according to the international standard ISO 5017:2013.

The crystal structures of the samples were examined with X-ray diffraction (XRD) by using a Bruker D5000 X-ray diffractometer. Phase search was performed using the EVA software and the International Center for Diffraction Data (ICDD) database PDF-2 Release 2003. In a few cases, it was necessary to change the lattice parameters from those used in the above references to achieve a better fit. The fitted lattice parameters are given shown in the results. Moreover, we show whether the phase detected in the samples has a major or a minor contribution to the peak of the diagram. A phase with a minor contribution has a peak with an amplitude smaller by approximately 20% than that of a major phase. Sometimes, we found it difficult to verify the presence of a minor phase is present because of the overlap between peaks. In this case, this minor phase was noted as dubious.

The micro Vickers hardness values of visually different phases in each sample were measured using a DuraScan 50 (Emco-Test). The diamond print was read directly read and converted into Vickers hardness. The load was 0.05 kgf.

3. Result

3.1. Structure and crystal structure

3.1.1 Sample A: left side of upper crust

A backscatter electron (BSE) image of the millimeter-scale entire-sample cross section and mappings of each of the elements, namely, Fe, U, Zr, Si, Al, and O, are shown in figure 2. The high intensity of a given color represents high content of the corresponding element in figure 2(b). The sample is composed of three zones: a narrow central zone containing large bubbles (approximately 0.3-1.2 mm) and two large side zones with a different microstructure and composition. The upper-side zone contains small bubbles (a few hundred microns,

sometimes coalesced). The bottom-side zone contains only one large bubble (1 mm), and it seems to be surrounded by large bubbles.

The microstructure of the left side of the bottom-side zone is shown in figure 3. Two types of dark matrix phases containing mainly Si and Fe are confirmed: one is the blight (dark) region denoted by 93 in figure 3, which has a eutectic-like microstructure; the second is the dark-gray region comprising silicon-rich nodules of the order of a dozen microns and denoted by 92 in figure 3. The Zr-rich phase, shown in bright-gray color and denoted by 94, and U-rich phases, shown in white color and denoted by 95, are observed in the matrix as well. These elemental fractions were determined by EDS analysis, and they are listed in table 1.

Similar microstructures and phases were found in the other bottom and upper zones in sample A. Five main phases were detected in these zones:

- A matrix of a Si- and Fe-rich oxide containing Na, Al, K, Zr, and U as minor elements.
- Small precipitates of a Si- and Fe-rich oxide measuring a few microns in size, richer in Si, Zr, and Ca than the matrix.
- Si-rich oxide nodules of different size, such as 2–3 μm or 10–15 μm in some areas, containing mainly Fe as the minor element.
- U- and Zr-rich oxide phase, richer in Zr, containing small amounts of Fe, which constitutes the main phase of the dendritic nodules in the matrix.
- U- and Zr-rich oxide phase, richer in U, often precipitated at the edge or in the Zr-rich oxide dendrites. It contains Fe and Si as well.

In the middle part of the sample, a few elements, namely, Al, Na, and Ca, were hardly observed compared to the case in the upper and the bottom zones. The mass fractions of Zr and U were significantly higher than those in the other zone. Phases similar to those in the other zone were detected in this zone.

The bulk density, ρ_b, and apparent porosity, π_a, of all samples are given in table 2. The differences between both values among the samples were small. The bulk density represents

the mixture of the dense initial corium and the light melted sacrificial concrete, and the apparent porosity represents the amount of voids in the sample. The fractions of the corium phase and the concrete phase, and void volume are similar across samples.

In the XRD analysis, two cubic-(U,Zr)O_2 phases and two similar tetragonal-ZrO_2 were detected as shown in figure 4(a) and given in table 3. According to the database, one phase of cubic-(U,Zr)O_2 should be $(U_{0.5},Zr_{0.5})O_2$ and the other one should be richer in Zr, based on its smaller lattice parameter. However, considering the results of the SEM analysis, we assumed that the actual uranium content of these phases is higher than that of the phases estimated from XRD analysis. This discrepancy might be ascribed to the insertion of minor elements in these phases, non-exact stoichimiometry of O, and errors in the database.

3.1.2 Sample B: center of upper crust

A general view of the millimeter-scale sample cross section in the form of BSE micrographs is shown in figure 5. The sample is rather homogeneous, and dendrites of corium phases are shown in white color. Many small bubbles, measuring less than 100 microns in diameter, are visible, and a few of these bubbles at the center of the samples are coalesced. A few larger bubbles measuring approximately 1 mm in diameter can be observed in the top right part of the sample. The presence of a small concrete-rich phase is confirmed along the right and upper edge.

In the microstructure of this sample, corium dendrites are precipitated in a concrete matrix. Examples of the microstructure are shown in figure 6. The results of elemental composition analysis of each phase by EDS are reported in table 4. The matrix is a Si- and Fe-oxide-rich phase with a Si-rich oxide phase constituted of round nodules, represented by black spots measuring 1–2 μm in diameter on the micrographs. The corium dendrites are composed of a Zr-rich oxide phase with a size of 12 microns or more. Small U-rich nodules, measuring a few microns or less in diameter and represented by white color on the

micrographs, are precipitated in these nodules or at the edges. Based on an analysis of all phases, five main phases were identified:

- A matrix of a Si- and Fe-rich oxide containing Zr, Al, K, Ca, and U.
- Small round precipitates, black dots measuring 1–2 μm in diameter, of Si-rich oxide containing Fe as the major element and Na, Al, Ca, Zr, and U as the minor elements.
- U- and Zr-rich oxide phase, richer in Zr and containing small amounts of Fe, which constitutes the main phase of the dendritic nodules precipitated in the matrix.
- U- and Zr-rich oxide phase, richer in U, often precipitated at the edge or in the Zr-rich oxide dendrites. It contains Fe and Si as well.
- A needle-like oxide, rich in Zr and Si, containing U and Fe as well; not shown in the figure.

In the XRD analysis, two types of cubic-$(U,Zr)O_2$ and tetragonal-ZrO_2 were detected unambiguously, as shown in figure 4(b) and given in table 3. Moreover, small peaks of monoclinic-ZrO_2 and cubic-$(Fe_xSi_y)_3O_4$ were detected, but their formations were unclear.

3.1.3 Sample C: right side of upper crust

The millimeter-scale structure of sample C, shown in figure 7, is a rather homogeneous corium zone, with small bubbles measuring <100 μm–400 μm in size. A different apparent zone without any bubbles and a small concrete film can be seen in the upper side of the sample. Concrete droplets can be seen as well, and their sizes are similar to those of the bubbles.

An example of the microstructures and phases encountered in the corium zone with bubbles is shown in figure 8. The results of elemental analyses by EDS are presented in table 5. Corium dendritic nodules measuring 10–50 μm with a brighter phase can be seen in the concrete-rich matrix shown in dark-gray color. The concrete-rich matrix contains black-dot phases measuring 1–3 μm in size. Four main phases were detected in this corium-rich zone:

- A matrix of Si- and Fe-rich oxide containing Zr, Al, K, Ca, and U.
- Small round precipitates of Si-rich oxide measuring 1–3 μm in size; containing Fe as the major alloying element; Na, Al, Ca, Zr, and U as the minor elements; and represented by black color.
- U- and Zr-rich oxide phase, richer in Zr and containing Fe, which constitutes the main dendritic nodules in the matrix.
- U- and Zr-rich oxide phase, richer in U, and often precipitated at the edge or in the Zr-rich oxide dendrites. It contains Fe and Si as well.

In the XRD analysis, a peak similar to that of sample A was found for sample C, as shown in figure 4(c). The main detected phases are two types of cubic-$(U,Zr)O_2$ and two similar tetragonal-ZrO_2 phases, as shown in table 3.

3.1.4 Sample D: inner region of molten pool

A general view of sample D in the form of BSE micrographs is shown in figure 9. This sample can be divided into two zones; corium-rich zone and concrete-rich zone. Only a few bubbles can be observed in this sample, and their diameters do not exceed 300 μm, except for one bubble with a diameter of 0.8 mm in the concrete-rich zone.

The microstructure of the corium-rich zone is similar to that of the corium-rich zones in the other samples. EDS analysis detected four main phases in the corium-rich zone:

- A matrix of a Si- and Fe-rich oxide containing Zr, Al, Ba, Ca, and U.
- Small round precipitates with black dots measuring 2–4 μm and consisting of Si-rich oxide with Fe as the major alloying element and Al, Ca, Zr, and U as the minor elements.
- U- and Zr-rich oxide phase, richer in Zr and containing Fe, which constitutes the main dendritic nodules in the matrix.
- U- and Zr-rich oxide phase, richer in U and often precipitated at the edge or in the Zr-rich oxide dendrites. It contains Fe and Si as well.

By contrast, the corium-poor zone has a quite heterogeneous microstructure with different contrasts of corium nodules. The corium phases form nodules measuring several dozens of micrometers in size, terminated by fine dendrites, as shown in figure 10. The results of the EDS elemental analyses are presented in table 6. The fractions of the nodules and fine dendrites differ according to the region. The matrix is a Si-rich oxide containing many minor elements: Na, Mg, Al, Ca, Fe, Zr, Ba, and U. The U-rich oxide is found only in the fine dendrites. The larger nodules are composed of the Zr-rich oxide phase.

The main phases in these zones are as follows:

- Si-rich oxide phase forming black round precipitates in the matrix or forming the matrix.
- Si- and Fe-rich oxide phase with mainly Ca and Al.
- Si- and Zr-rich oxide with a composition similar to that of the zircon phase, $ZrSiO_4$, containing U and Fe, but accurate phase identification is difficult because of its small size.
- Zr-rich oxide with U and a small amount of Fe forming large precipitates that measure dozens of microns in size.
- Small precipitates of U-rich oxide measuring approximately one micron in size and containing Zr, Fe, and Si.

In the XRD analysis, two types of cubic-$(U,Zr)O_2$ and two similar tetragonal-ZrO_2 were detected, as shown in figure 4(d) and given in table 3. However, the peak of one cubic-$(U,Zr)O_2$ in this sample was lower than those in the other samples.

3.2. Vickers hardness

The micro Vickers hardness values of all samples were measured in two types of phases: bright-gray corium phases and dark-gray concrete-rich matrix. It was assumed from the SEM-EDS analysis of the microstructure of each of the samples that the corium matrix is composed of a Zr-rich U- and Zr oxide phase, and the dark matrix is a Si- and Fe-rich oxide

phase or a Si-rich oxide phase. In each sample, four or five different zones were selected, and the hardness was measured between 3 and 14 times according to the homogeneity of the phases in each zone. The measurement results of each phase of each sample are shown in figure 11. The differences in the measured micro Vickers hardness values among the samples are small, but the differences between the two types of phases are relatively large.

4. Discussion

Four samples were taken from different locations on the large-scale MCCI test section, and their characteristics such as microstructure, crystal structure, and Vickers hardness were analyzed. We found rather small differences in the observed microstructure among the samples. This is one of the characteristics of the quenched MCCI product relative to the samples of VULCANO VBS-U4 [11]. The main reasons for the homogeneity among the samples are short melting time of less than 20 min and short cooling time owing to the use of a water-cooling system. The differences in cooling time between the upper crust region (samples A, B, and C) and the molten pool region (sample D) would be small, in spite of the differences in surface appearance.

In all samples, the presence of many bubbles was confirmed. Bubbles are links to porosity in the sample, and porosity influences mechanical properties. UO_2 fuel pellets with higher porosity have lower micro Vickers hardness, Young's modulus [15], and fracture toughness [16]. The measured apparent porosities of the VW-U1 samples, as given in table 2, are lower than those of the VBS-U4 samples, except for sample D1 [11]. Small concrete ablation of VW-U1 affected lower apparent porosity, and higher micro Vickers hardness in comparison to that of the VBS-U4 sample, which is described later. The bubbles in the VW-U1 samples would have been formed mainly by the water vapor from the ablated sacrificial concrete at the bottom of the concrete test section. This is because metals such as Zr and Fe, which can reduce concrete components, were not used in the initial corium, and the

generation of a reduction gas phase, such as H_2 and CO, was limited [12, 17]. Moreover, the generation of concrete decomposition gases such as CO_2 was limited because $CaCO_3$ was not included in the sacrificial concrete [12, 18]. These are among the reasons for the less apparent porosity.

Chemical phase is the parameter with the strongest influence of the material properties of the samples. The main difference in the chemical phases detected by XRD between the VW-U1 and the VBS-U4 samples, except for the metallic phase in VBS-U4, is the presence or absence of a zircon phase, $ZrSiO_4$, and a SiO_2-based crystal phase, such as cristobalite or quartz. These phases were detected only in the VBS-U4 samples [11]. In general, the crystal structure is composed of molten SiO_2 depending on cooling time, and the amorphous SiO_2 phase is produced under quenching. In the case of XRD measurement of the SiO_2 amorphous phase, a sharp peak was not detected in the spectrum, but a broad peak was detected around 2 θ = 23° [19]. In the present study, a peak around $2\theta = 23°$ was not detected in the measured spectrum, as shown in figures 4. It is expected that the contents of the SiO_2 phase are too minor to be detected using XRD, despite the detection of SiO_2-based phases in the SEM-EDS analysis, because only a small amount of ablated concrete mixed with the molten pool. The reason for the lack of formation of the zircon phase, as confirmed by XRD, was limited formation of the SiO_2 crystal phase, which changes to zircon phase in the presence of ZrO_2 phase.

In general, only one cubic-$(U,Zr)O_2$ phase is formed when the ZrO_2 fraction in $(U,Zr)O_2$ is smaller than approximately 50 mol% and $(U,Zr)O_2$ is quenched from the temperatures higher than 1900 K [20-21]. The molar fraction of ZrO_2 in UO_2 and ZrO_2 in the initial corium in this experiment was approximately 50 mol%; if the initial corium temperature were higher than 2000 K, significant amounts of cubic-$(U,Zr)O_2$ with high ZrO_2 contents could be formed under quenching. In fact, not only two types of cubic-$(U,Zr)O_2$ but also two different types of ZrO_2 were detected in the XRD analysis of samples A, B, and C. It

is expected from the UO_2 and ZrO_2 phase diagram [20] and their microstructures that cubic-$(U_{0.5},Zr_{0.5})O_2$ can be divided into a U-rich $(U,Zr)O_2$ phase and a Zr-rich $(U,Zr)O_2$ phase at temperatures of approximately 1800 K. The temperature in the upper part of the molten pool would remain close to this temperature before quenching, and subsequently, the molten pool would be cooled by quenching. By contrast, one cubic-$(U,Zr)O_2$ phase was mainly formed in sample D according to the XRD analysis. Here, in the inner region of the molten pool, the temperature could be higher than that in the upper region, and the inner region was cooled by quenching.

The Vickers hardness of the corium phase in the VW-U1 samples was higher than the corresponding values in case of the VBS-U4 samples [11], melted $(U,Zr)O_2$ produced by plasma arc furnace [22], and sintered pellets of cubic $(U,Zr)O_2$ [21]. The differences in Vickers hardness between the VW-U1 and VBS-U4 samples can be ascribed to differences in measurement conditions and microstructures. The microstructure of the VBS-U4 oxide samples is more heterogeneous than that of the VW-U1 samples, and higher pressing force during VBS-U4 measurements could have affected the softer concrete phases around the corium phases. Moreover, quenching could be the cause of the rather small porosity, as given in table 2; low fraction of concrete components owing to limited concrete ablation; and presence of a large amount of Zr-rich $(U,Zr)O_2$ in the VW-U1 samples. Because of this composition, the VW-U1 samples had higher micro hardness. By Contrast, the Vickers hardness values of the concrete-rich phases in the VW-U1 samples were higher than the corresponding values of the VBS-U4 samples. The higher Vickers hardness of the former samples can be ascribed to the quenching condition. The Vickers hardness of the concrete phase in the inner region of the molten pool, sample D, was the lowest in this measurement, and it can be ascribed to the relatively slow cooling rate and small differences in crystalline structure compared to that in the other regions.

From a comparison of the VW-U1 samples produced under the quenching condition

with the VBS-U4 samples produced under the gently cooled condition, it was assumed that the MCCI product generated under the quenching condition would be homogeneous, and its hardness would be higher than that of the inner region of the MCCI product.

5. Conclusion

Samples from a large-scale MCCI test performed under quenching conditions, VULCANO VW-U1, were analyzed to evaluate the characteristics of the surface of the MCCI product just below the cooling water generated in 1F. The samples were homogeneous, despite being taken from different locations in the test section. Several corium phases, such as cubic-$(U,Zr)O_2$ and tetragonal ZrO_2, were detected by XRD analysis, but concrete-based phases such as crystalline SiO_2 phase were not detected because the fractions of the SiO_2 -based phases were limited in the analysis. The Vickers hardness value of each phase in these samples was higher than values of the corresponding phases in the samples obtained from another VULCANO test campaign, VBS-U4. The quenching condition was thought to influence the microstructure of the samples, such as lower fraction of concrete phases, lower porosity, and higher hardness.

References

[1] Yano K, Kitagaki T, Ikeuchi H, Wakui R, Higuchi H, Kaji N, Koizumi K, Washiya T. Direction on characterization of fuel debris for defueling process in Fukushima Daiichi nuclear power station. Proc. GLOBAL 2013; 2013 Sep 29-Oct 3; Salt Lake City (United States). p.1554-1559.

[2] Upgrading level of grasping state inside reactor (project of decommissioning and contaminated water management). Japan: International Research Institute for Nuclear Decommissioning, The Institute of Applied Energy; 2018. available from http://irid.or.jp/_pdf/20170000_01.pdf [in Japanese]

[3] Pazukhin ÉM. Fuel-containing lavas of the Chernobyl NPP fourth block: Topography, physicochemical properties, and formation scenario. Radiochem. 1994 Mar-Apr; 36(2):109-154.

[4] Burakov BE, Ojovan MI, Lee WE. Crystalline materials for actinide immobilization. London: Imperial college press; 2010. p.73-83.

[5] Shiryaev AA, Vlasova IE, Burakov BE, Ogorodnikov BI, Yapaskurt VO, Averin AA, Pakhnevich AV, Zubavichus YV. Physico-chemical properties of Chernobyl lava and their destruction product. Prog. Nucl. Energy. 2016 Sep; 92:104-118.

[6] Kitagaki T, Yano K, Ogino H, Washiya T. Thermodynamic evaluation of the solidification phase of molten core-concrete under estimated Fukushima Daiichi nuclear power plant accident conditions. J. Nucl. Mat. 2017 jan; 486:206-215.

[7] Foit JJ, Fischer M, Journeau C, Langrock G. Experiments on MCCI with oxide and steel. Ann. Nucl. Energy. 2014 Dec; 74:100-109.

[8] Journeau C, Sudreau F, Magne S, Cognet G. Physico-chemical analyses and solidification path reconstruction of multi-component oxidic spread melts. Mat. Sci. Eng.:A 2001 Jan; 299(1-2):249-266.

[9] Journeau C, Piluso P, Haquet JF, Boccaccio E, Saldo V, Bonnet JM, Malaval S, Carénini L, Brissonneau L. Two-dimensional interaction of oxidic corium with concretes: The VULCANO VB test series. Ann. Nucl. Energy. 2009 Oct; 36(10):1597-1613.

[10] Sevón T, Journeau C, Ferry L. VULCANO VB-U7 experiment on interaction between oxidic corium and hematite-containing concrete. Ann. Nucl. Energy. 2013 Sep; 59:224-229.

[11] Kitagaki T, Ikeuchi H, Yano K, Ogino H, Haquet JF, Brissoneau L, Tormos B, Piluso P, Washiya T. Characterization of the VULCANO test products for fuel debris removal from the Fukushima Daiichi nuclear power plant. Prog. Nucl. Sci. Tech. 2018 Dec; 5:217-220.

[12] Journeau C, Alsmeyer H. Validation of the COMET bottom-flooding core-catcher with prototypic corium, Proc. ICAPP2006; 2006 Jun 4-8; Reno (United States). p.1314-1321.

[13] Journeau C, Piluso P, Correggio P, Ferry L, Fritz G, Haquet JF, Monerris J, Ruggieri JM, Sanchez-Brusset M, Parga C. Contributions of the vulcano experimental programme to the understanding of mcci phenomena, Nucl. Eng. Tech. 2012 Apr; 44 (3):261-272.

[14] Alsmeyer H, Cron T, Merkel G, Schmidt-Stiefel S, Tromm W, Wenz T. Melt Cooling by Bottom Flooding: The Experiments CometPC-H4 and -H5. Germany: FZK; 2004, Report SAM-ECOSTAR-D45.

[15] Cappia F, Pizzocri D, Marchetti M, Schubert A, Uffelen PV, Luzzi L, Papaioannou D, Macián-Juan R, Rondinella V.V. Microhardness and Young's modulus of high burn-up UO_2 fuel. J. Nucl. Mat. 2016 Oct; 479:447-454.

[16] Oguma M. Microstructure effects on fracture strength of UO_2 fuel pellets. J. Nucl. Sci. Tech. 1982 Dec; 19(12):1005-1014.

[17] Alsmeyer H, Adelhelm C, Dillman HG, Foit JJ, Heinle M, Ratajczak W, Schneider H, Schumacher G, Skokan A, Stiefel S, Tromm W. BETA experiments on melt-concrete interaction: the role of zirconium and the potential sump water contact during core melt-down accidents. Nucl. Eng. Des. 1995 Feb; 154(1):61-68.

[18] Journeau C, Piluso P. Core concrete interaction. Netherlands: Elsevier science; 2012, Comprehensive nuclear materials vol.2 2.25; 635-654.

[19] Musić S, Filipović-Vinceković N, Sekovanić L. Precipitation of amorphous SiO_2 particles and their properties. Brazilian J. chem. eng. 2011 Jan-Mar; 28(1):89-94.

[20] Chevalier PY, Fischer E, Cheynet B. Progress in the thermodynamic modeling of the O-U-Zr ternary system. Comp. Coup. Phase. Diag. Therm. 2004 Apr; 28:15–40.

[21] Kitagaki T, Hoshino T, Yano K, Okamura N, Ohara H, Fukasawa T, Koizumi K. Mechanical properties of cubic $(U,Zr)O_2$. J. Nucl. Eng. Rad. Sci. 2018 Jul; 4:031011.

[22] Takano M, Nishi T, Shirasu N. Characterization of solidified melt among materials of

UO_2 fuel and B_4C control blade. J. Nucl. Sci. Tech. 2014 May; 51(7-8):859-875.

Figure captions

Table 1 EDS analysis of phases in corium-rich zone in sample A

	92		93		94		95	
Element	at.%	wt.%	at.%	wt.%	at.%	wt.%	at.%	wt.%
O	56.9	36.4	50.1	27.9	56.6	14.1	59.2	11.1
Na	0.7	0.6	-	-	-	-	-	-
Al	0.6	0.7	0.6	0.5	-	-	-	-
Si	35.4	39.7	25.4	24.7	-	-	4.1	1.4
K	0.5	0.8	0.4	0.5	-	-	-	-
Ca	0.4	0.7	-	-	-	-	-	-
Fe	3.9	8.6	23	44.5	2	1.7	3.4	2.2
Zr	0.5	1.7	0.4	1.2	30.2	42.8	4.2	4.4
U	1.1	10.8	0.1	0.7	11.2	41.4	29.1	80.9

Table 2 Bulk density, ρ_b, and apparent porosity, π_a, of all samples

Samples	A	B	C	D
ρ_b [g/cm^3]	5.44	5.53	5.51	5.60
π_a [%]	3.17	3.22	3.61	2.31

Table 3 Phases detected in each sample by XRD measurement

Phase (ICDD PDF-2 ID)	Lattice parameters (Å)	Sample A	Sample B	Sample C	Sample D
Cubic-$(U_{0.5},Zr_{0.5})O_2$ (78-0665)	a= 5.42	Major +	Major	Major	Major
Cubic-$(U, Zr)O_2$* (78-0665)	a= 5.3963	Major	Major +	Major +	-
Cubic-$(U, Zr)O_2$* (78-0665)	a= 5.285	-	-	-	Minor
Tetragonal-ZrO_2* (24-1164)	a= 3.6593, c= 5.27	Major +	-	-	-
Tetragonal-ZrO_2* (24-1164)	a= 3.687, c= 5.27	Major	-	-	-
Tetragonal-ZrO_2* (24-1164)	a=3.6493, c=5.2442	-	Major +	-	-
Tetragonal-ZrO_2* (24-1164)	a=3.6479, c=5.2483	-	-	Major +	-
Tetragonal-ZrO_2* (24-1164)	a= 3.6877, c= 5.27	-	-	Major	-
Tetragonal-ZrO_2* (24-1164)	a= 3.655, c= 5.2462	-	-	-	Major
Tetragonal-ZrO_2* (24-1164)	a= 3.6593, c= 5.27	-	-	-	Major
Monoclinic-ZrO_2* (89-9066)	a= 5.0718, b= 5.205, c= 5.33, β = 99.37	-	Dubious	-	-
$(Fe_{0.324}Si_{0.676})(Fe_{0.963}Si_{0.037})_2O_4$ (89-6229)	a= 8.286	-	Dubious	-	-

When the lattice parameters were changed from the ICDD database PDF-2 to obtain a better fit, the phase was marked with an asterisk, *.

Table 4 EDS analysis of phases in corium-rich zone in sample B

	41		42		43		44	
Element	at.%	wt.%	at.%	wt.%	at.%	wt.%	at.%	wt.%
O	57.7	37.5	53.1	30.0	59.1	15.4	62.8	16.5
Na	0.5	0.4	-	-	-	-	-	-
Al	0.3	0.4	0.4	0.4	-	-	-	-
Si	32.1	36.5	24.3	24.0	-	-	11.2	5.1
K	0.5	0.8	0.3	0.3	-	-	-	-
Ca	0.6	0.9	1.4	2.0	-	-	-	-
Fe	6.8	15.4	19.2	37.7	1.7	1.5	3.4	3.1
Zr	1.0	3.6	1.0	3.3	28.9	43.0	5.3	7.8
U	0.5	4.5	0.3	2.3	10.3	40.1	17.3	67.5

Table 5 EDS analysis of phases in corium-rich zone in sample C

	136		137		138		139	
Element	at.%	wt.%	at.%	wt.%	at.%	wt.%	at.%	wt.%
O	55.1	37.3	50.2	27.5	59.5	15.5	63.2	14.2
Na	0.5	0.4	-	-	-	-	-	-
Al	0.4	0.5	0.4	0.4	-	-	-	-
Si	38.3	45.3	24.5	23.5	-	-	7.2	2.8
K	0.5	0.8	-	-	-	-	-	-
Ca	0.3	0.5	1.5	2.1	-	-	-	-
Fe	3.8	9	22.3	42.6	1.7	1.5	2.8	2.2
Zr	0.7	2.5	0.9	2.7	27.9	41.2	4.3	5.5
U	0.4	3.7	0.2	1.2	10.9	41.8	22.5	75.3

Table 6 EDS analysis of phases in concrete rich-zone in sample D

	26		27		28		29	
Element	at.%	wt.%	at.%	wt.%	at.%	wt.%	at.%	wt.%
O	54.8	30.4	59.5	16	61.7	14.5	61.5	18.9
Na	3.6	2.8	-	-	-	-	1.3	0.6
Mg	0.4	0.3	-	-	-	-	-	-
Al	1.4	1.3	-	-	-	-	0.9	0.5
Si	27.5	26.6	-	-	-	-	11.1	6
Ca	2.7	3.7	-	-	-	-	1.6	1.3
Fe	3.4	6.5	1.4	1.3	1.6	1.3	1.6	1.7
Zr	3.5	10.9	30.1	46.4	20.4	27.3	10.3	18.2
Ba	1.3	6.1	-	-	-	-	0.5	1.3
U	1.4	11.4	9	36.3	16.3	56.9	11.2	51.5

Color Print

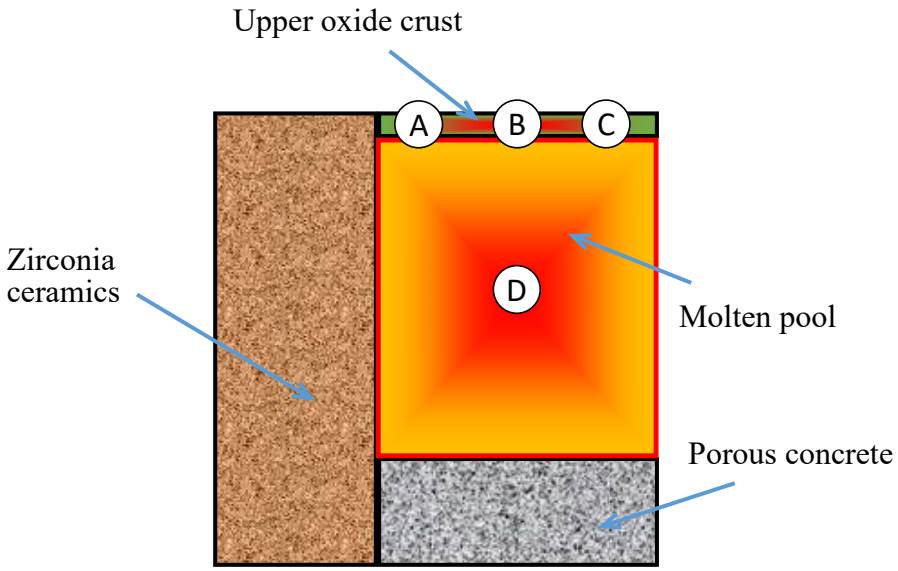

Figure 1. Schematic cut view of VW-U1 test section and sample location

Color Print

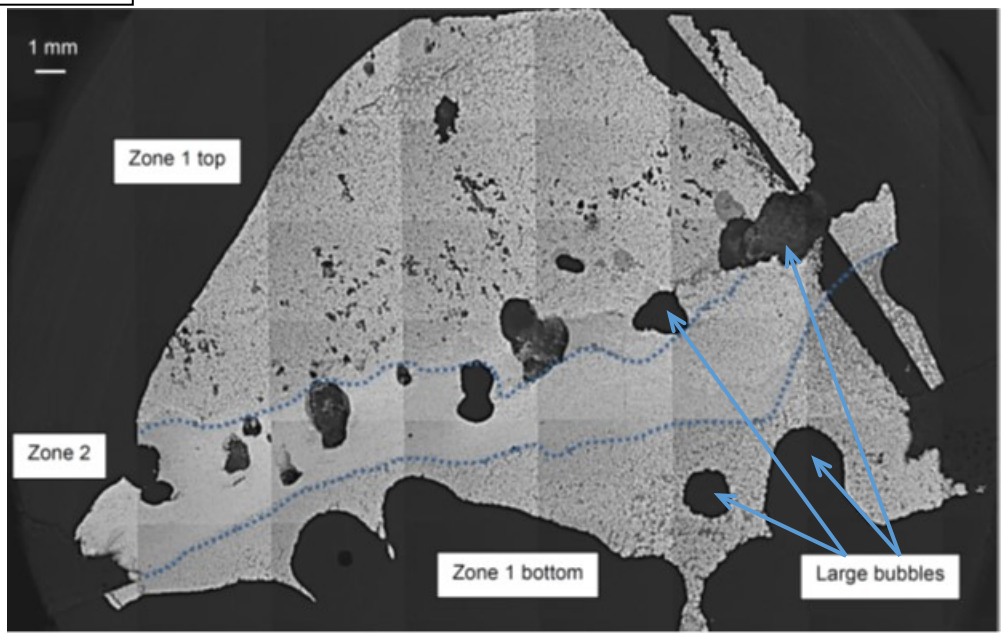

(a) Backscatter electron image of sample A cross section

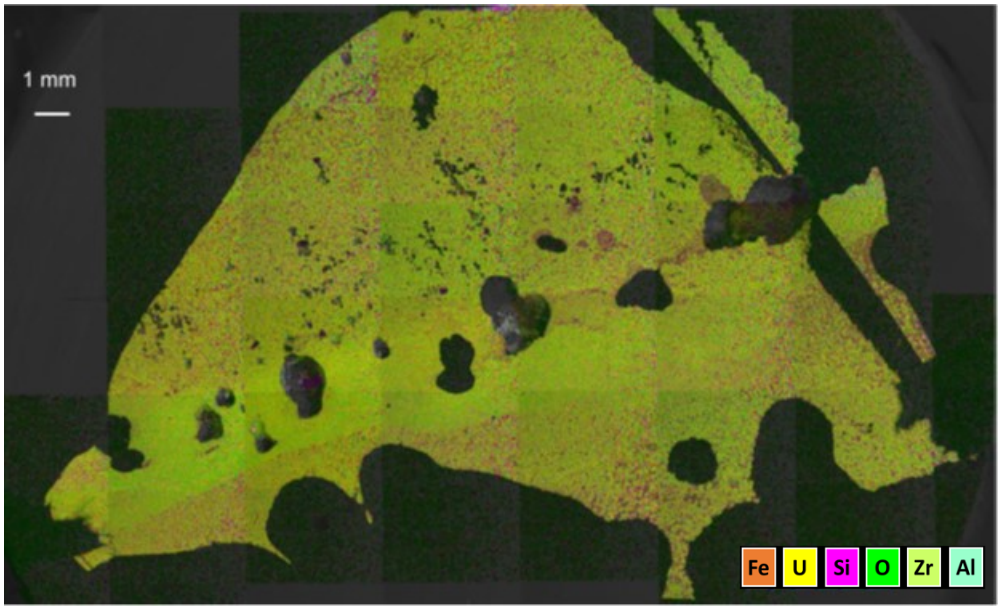

(b) Elemental mapping of sample A cross section

Figure 2. Backscatter electron image and elemental mapping of sample A cross section

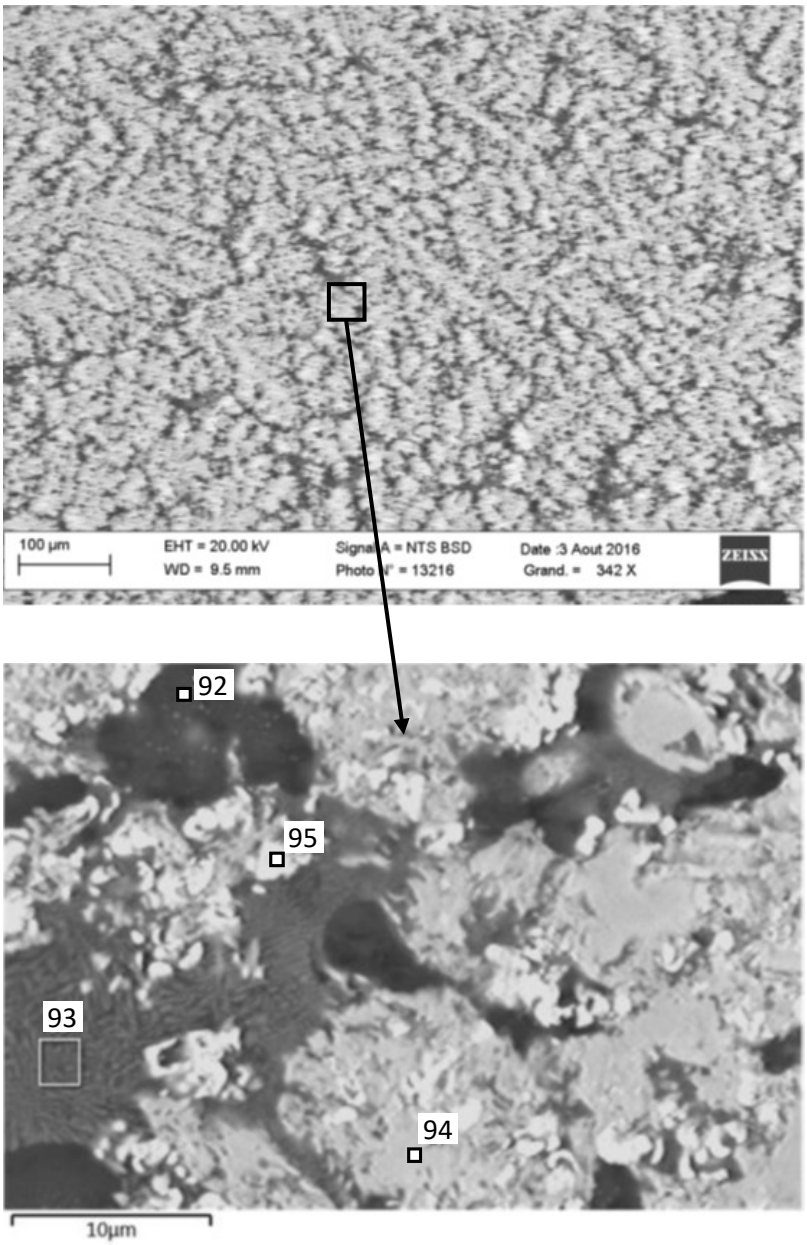

Figure 3. Backscatter electron image of microstructure of bottom left side zone in sample A

Color Print

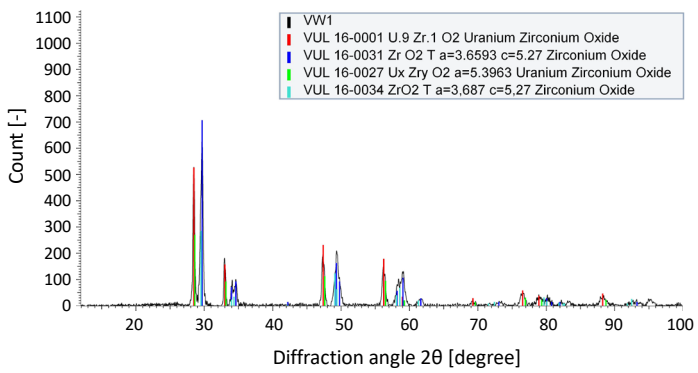

(a) Sample A

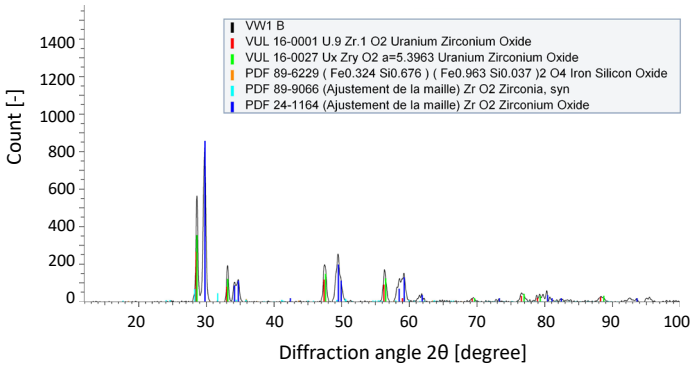

(b) Sample B

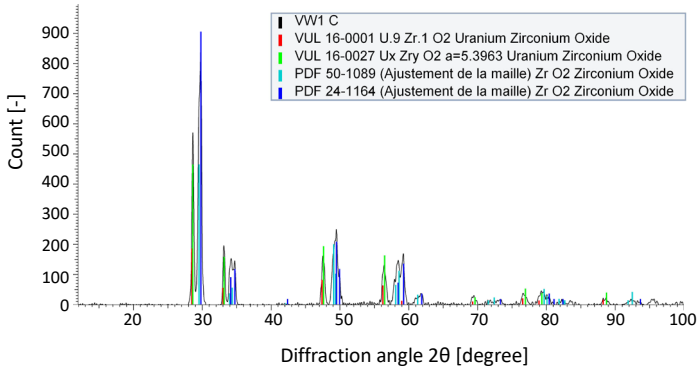

(c) Sample C

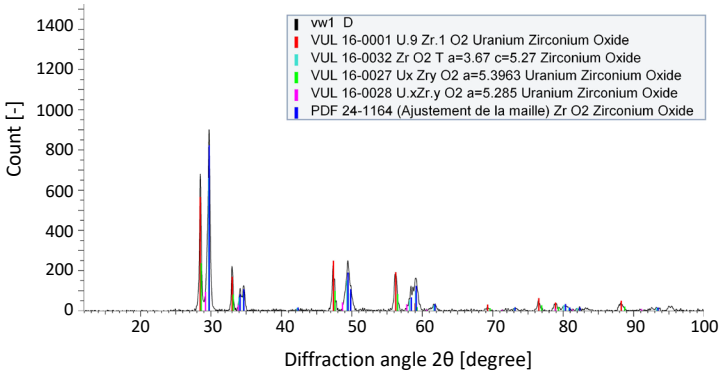

(d) Sample D

Figure 4. X-ray diffraction patterns of samples and phases detected in them

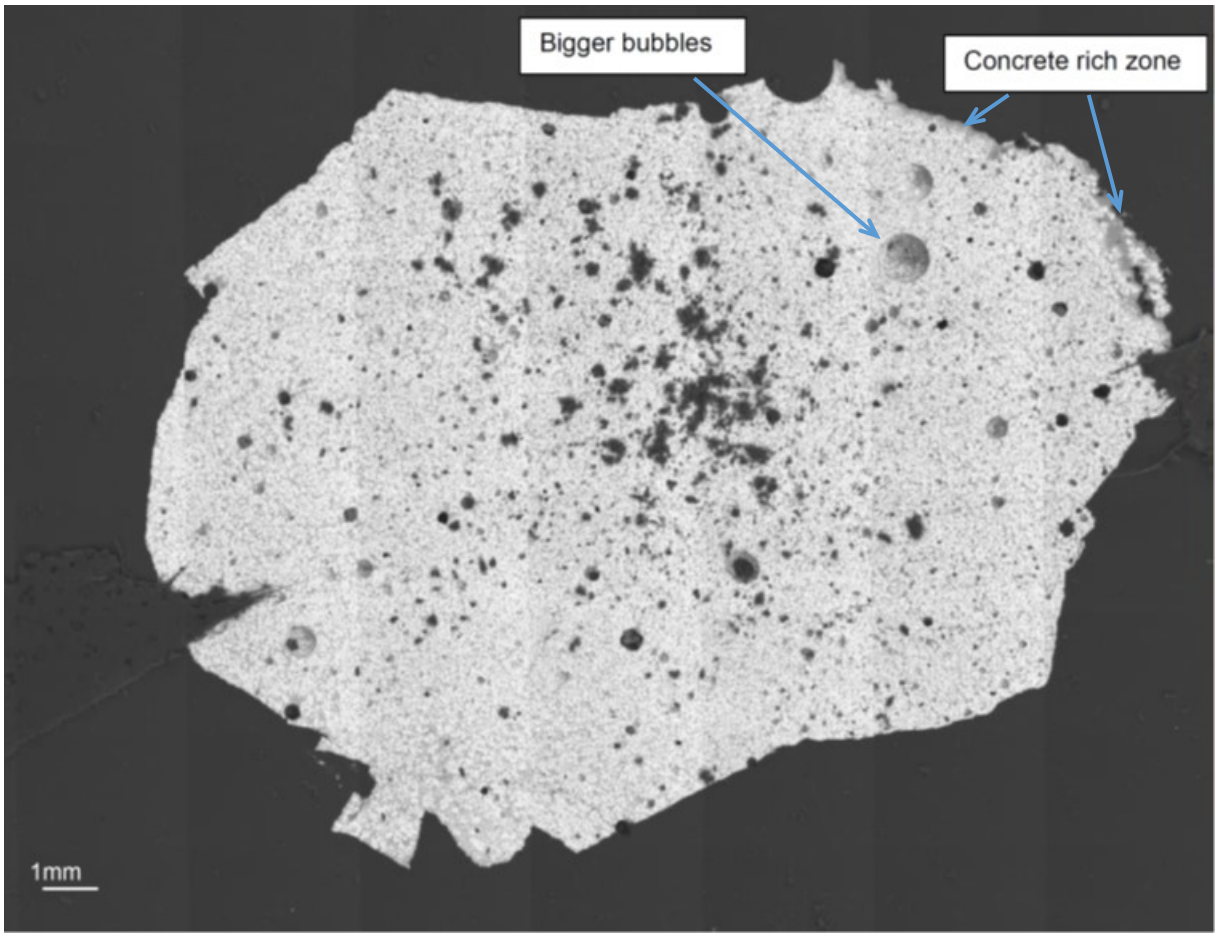

Figure 5. Backscatter electron image of sample B cross section

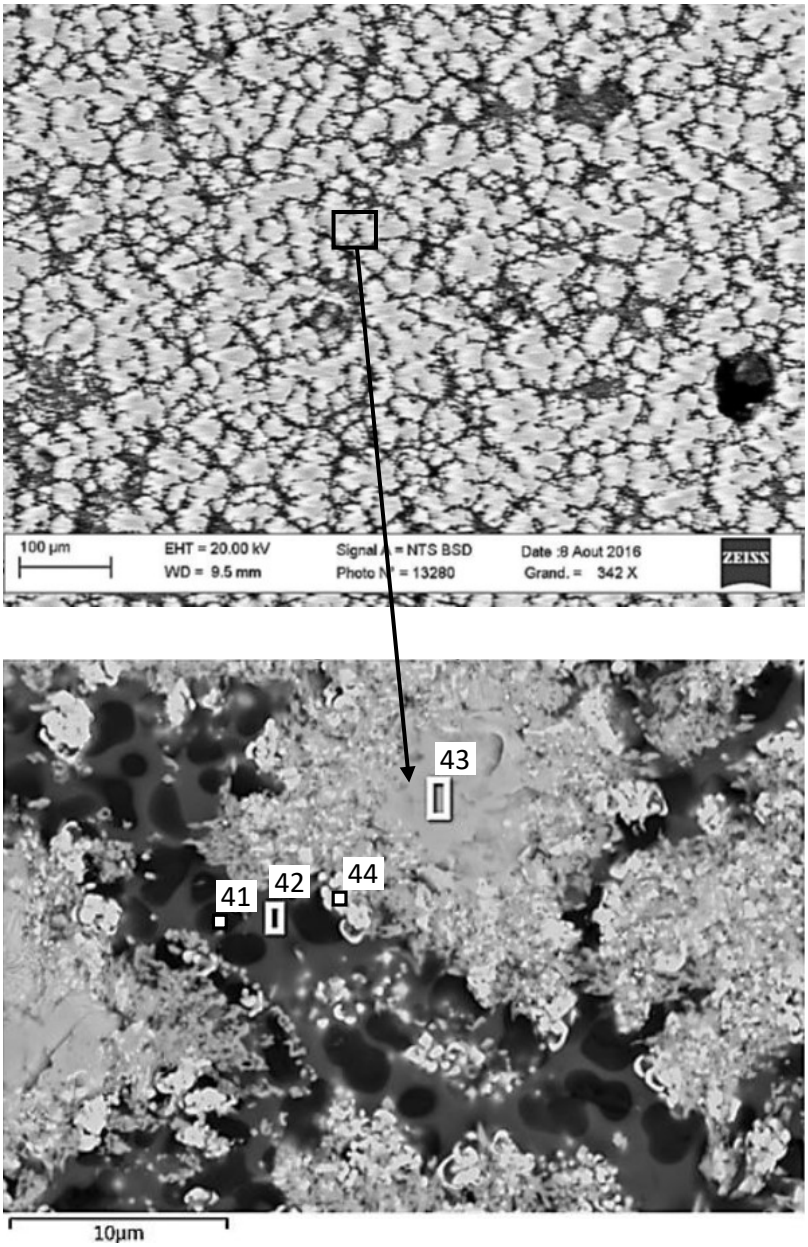

Figure 6. Microstructure and locations of phase analyses in sample B

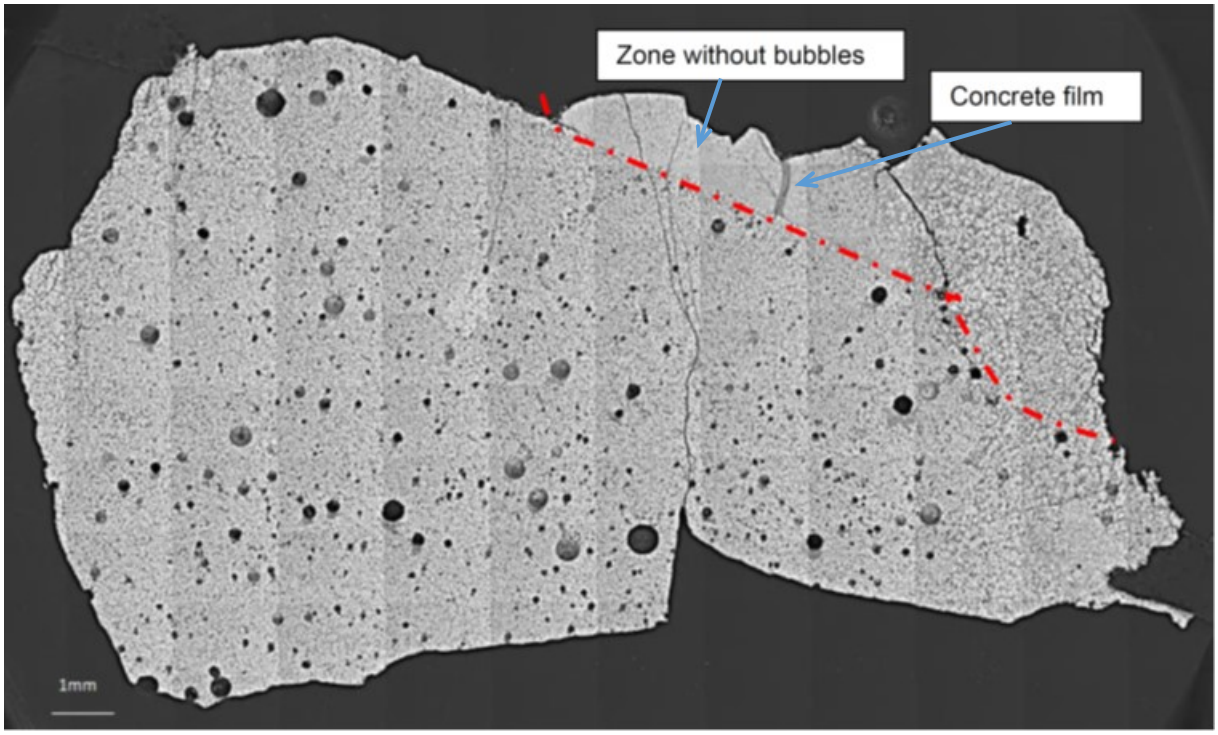

Figure 7. Backscatter electron image of sample C cross section

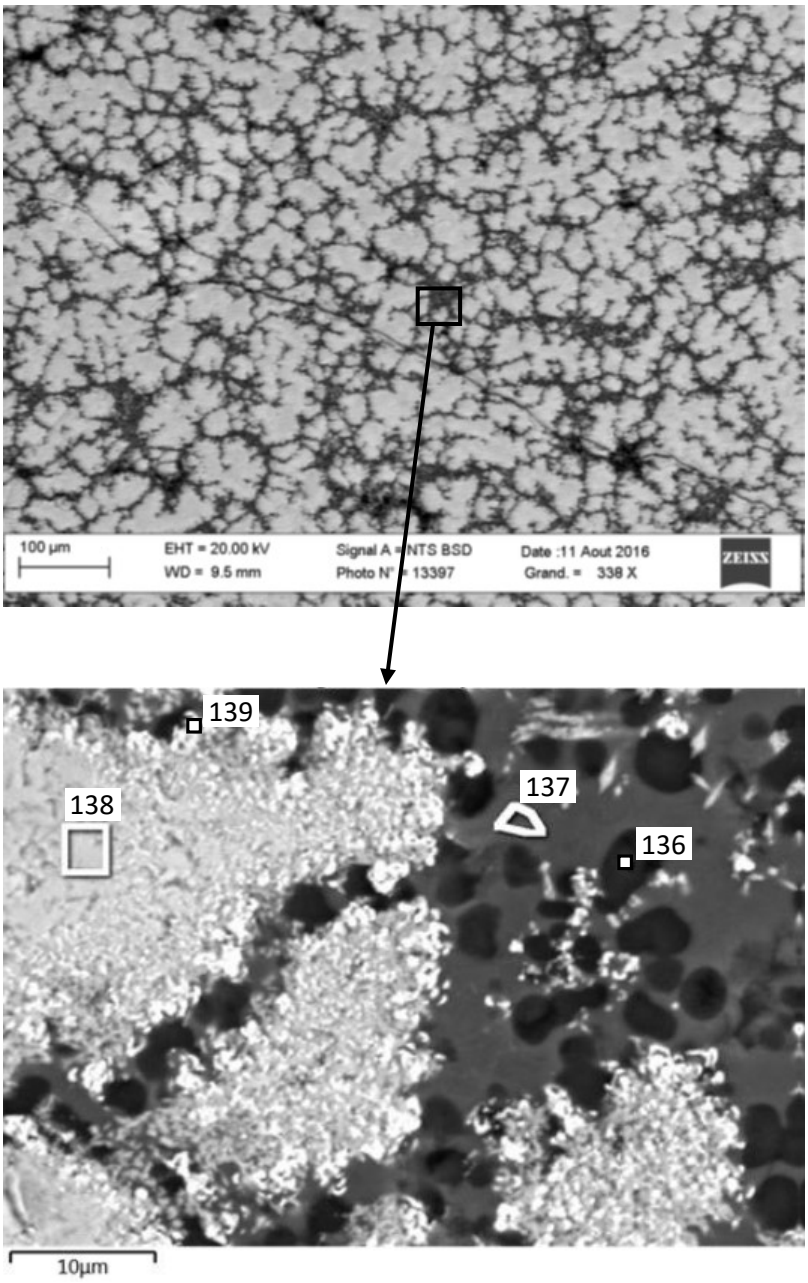

Figure 8. Microstructure and locations of EDS phase analyses in corium-rich zone in sample C

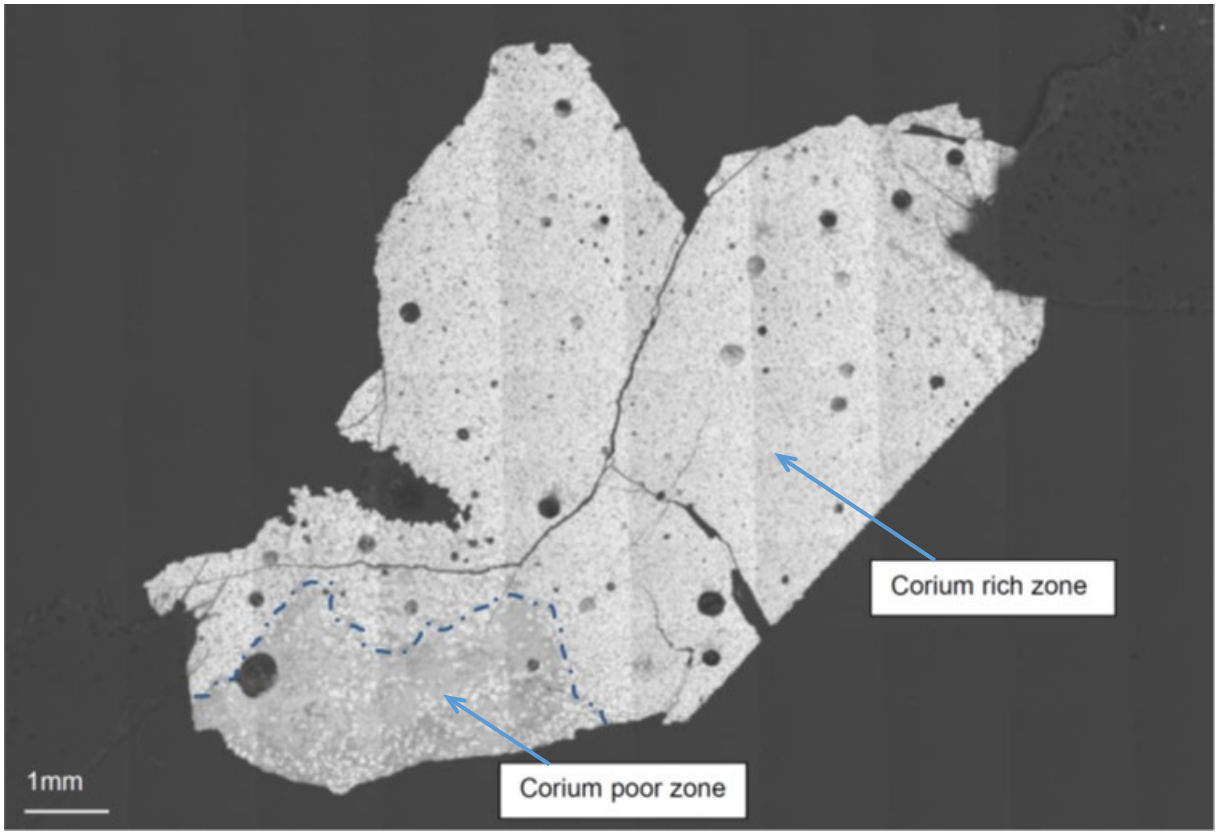

Figure 9. Backscatter electron image of sample D cross section

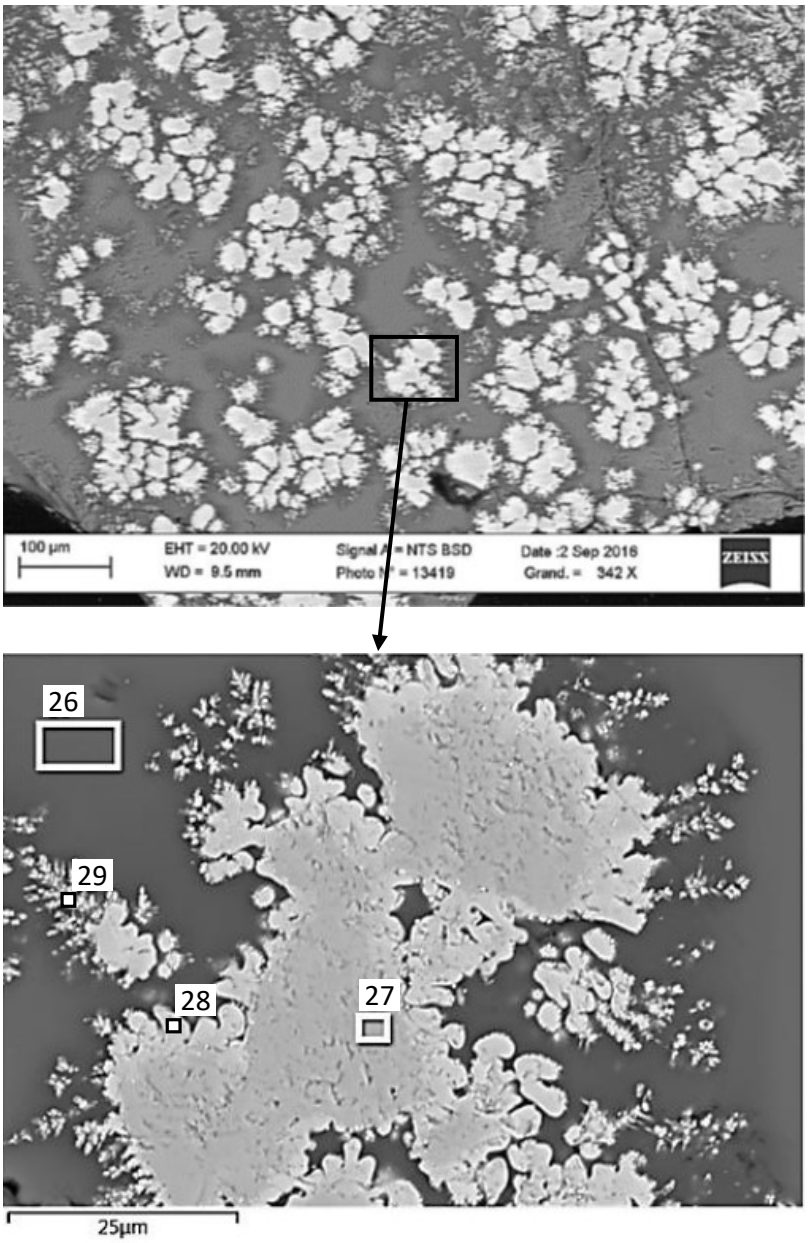

Figure 10. Microstructure and locations of EDS phase analyses in corium-poor zone in sample D

Color Print

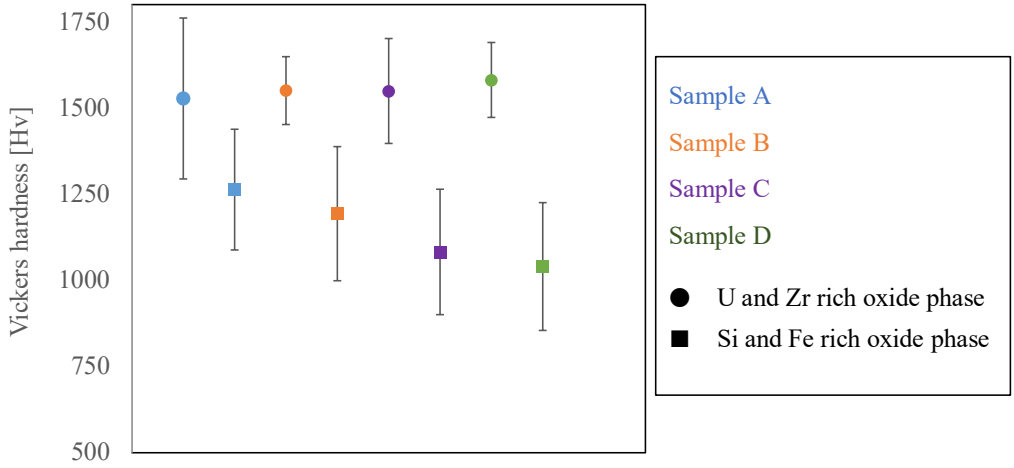

Figure 11. Measurement results of micro Vickers hardness in two types of phases in each sample

T. Kitagaki:

Effect of quenching on molten core-concrete interaction product